

Identification of flexible Pif1–DNA interactions and their impacts on enzymatic activities

Jinghua Li^{1,†}, Jianbing Ma^{1,2,†}, Vikash Kumar^{3,†}, Hang Fu^{4,6}, Chunhua Xu¹, Shuang Wang¹, Qi Jia^{1,2}, Qinkai Fan^{1,6}, Xuguang Xi⁵, Ming Li^{1,2,6}, Haiguang Liu^{3,*} and Ying Lu^{1,2,6,*}

¹Beijing National Laboratory for Condensed Matter Physics, Institute of Physics, Chinese Academy of Sciences, Beijing 100190, China, ²Songshan Lake Materials Laboratory, Dongguan, Guangdong 523808, China, ³Complex Systems Division, Beijing Computational Science Research Center, Beijing 100193, China, ⁴Wenzhou Institute, University of Chinese Academy of Sciences, Wenzhou, Zhejiang 325011, China, ⁵Laboratoire de Biologie et Pharmacologie Appliquée (LBPA), UMR8113 CNRS, ENS Paris-Saclay, Université Paris-Saclay, Gif-sur-Yvette F-91190, France and ⁶School of Physics, University of Chinese Academy of Sciences, Beijing 100049, China

Received December 12, 2021; Revised May 31, 2022; Editorial Decision June 02, 2022; Accepted June 07, 2022

ABSTRACT

Flexible regions in biomolecular complexes, although crucial to understanding structure–function relationships, are often unclear in high-resolution crystal structures. In this study, we showed that single-molecule techniques, in combination with computational modeling, can characterize dynamic conformations not resolved by high-resolution structure determination methods. Taking two Pif1 helicases (ScPif1 and BsPif1) as model systems, we found that, besides a few tightly bound nucleotides, adjacent solvent-exposed nucleotides interact dynamically with the helicase surfaces. The whole nucleotide segment possessed curved conformations and covered the two RecA-like domains of the helicases, which are essential for the inch-worm mechanism. The synergetic approach reveals that the interactions between the exposed nucleotides and the helicases could be reduced by large stretching forces or electrostatically shielded with high-concentration salt, subsequently resulting in reduced translocation rates of the helicases. The dynamic interactions between the exposed nucleotides and the helicases underlay the force- and salt-dependences of their enzymatic activities. The present single-molecule based approach complements high-resolution structural methods in deciphering the molecular mechanisms of the helicases.

INTRODUCTION

Structure–function relationships are the foundation of molecular biology, based on which enzymatic activities can be understood (1–3). However, it is challenging to directly assess structure–function relationships using conventional biochemical and biophysical methods, especially for DNA-interacting enzymes (4–7). Conformational fluctuations in highly flexible structural domains may either make the enzymes difficult to crystallize for high-resolution crystallography studies or result in blurred electron density maps in those highly flexible regions (8–12). On the other hand, most functional assays provide little information about structures and, therefore, cannot yield a direct structure–function correspondence. Therefore, it is essential to combine information from multiple sources for a comprehensive understanding of molecular structures and dynamics.

DNA helicases engage single-stranded DNA (ssDNA), whose binding modes play a pivotal role in their enzymatic activities. Inch-worm mechanisms were proposed to explain the translocation of non-ring-shaped helicases along ssDNA, in which the helicases move by alternating affinities between RecA-like domains (1A and 2A) and ssDNA at different stages of the adenosine triphosphate (ATP) hydrolysis cycle (10,13). The lack of high-resolution structure for the nucleotides that are not tightly bound to the helicase can be due to the dynamic nature of the flexible regions, which may possess multiple conformations. Even though these nucleotides are linked to the co-crystallized nucleotides that are tightly bound by the helicase, their structures cannot be directly determined from the X-ray crystallography or Cryo-EM methods (8–12,14). We denote these exposed nucleotides as ‘the adjacent nucleotides’, meaning

*To whom correspondence should be addressed. Tel: +86 10 82648122; Email: yinglu@iphy.ac.cn

Correspondence may also be addressed to Haiguang Liu. Tel: +86 10 56981816; Email: hgliu@csr.ac.cn

†The authors wish it to be known that, in their opinion, the first three authors should be regarded as Joint First Authors.

that they are directly connected to the co-crystallized segment. The ssDNA structures in a large proportion of the DNA–helicase complexes documented in the Protein Data Bank (PDB) are often limited to short segments that are tightly bound by the helicases (Supplementary Table S1). For instance, the electron density of ssDNA beyond the fifth nucleotide (nt) in the 3′-loading tail is blurry in the plasmid copy reduced (PcrA)–DNA complex, providing little information about the ssDNA–A1 domain interaction (Supplementary Figure S1A) (10). In the structure of Bloom’s syndrome helicase (BLM)–DNA complex, only about four or five fully bound nucleotides in the loading tail have been resolved (Supplementary Figure S1B and C) (15,16). We and others crystallized Pif1 helicases with six nucleotides that are fully bound by Pif1 (Supplementary Figure S1D and E) (8,9,11,12,14). In this work, we focus on two Pif1 helicases of SF1B superfamily. The Pif1 helicases are from *Saccharomyces cerevisiae* and *Bacteroides* sp. (ScPif1 and BsPif1), belonging to a eukaryotic organism and a prokaryotic organism respectively. These two helicases are among the model systems that are widely studied. They translocate in the 5′ to 3′ direction and participate in various nucleic acid metabolism processes, such as Okazaki fragment processing (17,18), break-induced replication (19,20), and telomerase regulation (21,22). The lack of structural information about the adjacent nucleotides makes it difficult to characterize the interaction of ssDNA with the RecA-like domains. Therefore, it is challenging to explain the enzymatic activities of the helicases solely based on high resolution structures of these complexes (23–26).

Single-molecule approaches, assisted by computational modeling, are becoming important complementary tools to conventional structure determination methods. Single-molecule fluorescence resonance energy transfer (smFRET) can continuously track the dynamic structural signals of individual biomolecules at functionally relevant timescales. However, smFRET can probe information about distances among only a few labeled sites of the biomolecules. In contrast, computational simulations offer an *in silico* approach to examining the details of biomolecular structures and dynamics, although the timescales are often limited by computing resources and the protocols employed in the simulations. In this study, using computational modeling/simulation, smFRET, and magnetic tweezers (MTs), we obtained critical structural information for the flexible nucleotides that are missing in crystal structures, based on which we hypothesized and validated the effects of force and salt concentration on the activities of two Pif1 helicases mentioned previously, ScPif1 (8) and BsPif1 (9).

MATERIALS AND METHODS

Pif1 purification

The plasmid encoding the yeast *Pif1* gene was kindly provided by Dr. Zakian. The purification of the ScPif1 protein (237–780) was performed as previously described (27), with minor modifications, while the BsPif1 protein purification was performed as previously described (28).

DNA constructs

DNA substrates were prepared using oligonucleotides, which were purified with ultrapage method by Sangon Biotech Co., Ltd (Shanghai, China), from whom we ordered the purified oligonucleotide products. The structure and sequence of each DNA construct are described in Supplementary Tables S2 and S3 and in Supplementary Figure S2. DNA was annealed at 95°C for 5 min and then slowly cooled down to room temperature for ~7 h. Annealing was executed in the buffer containing 50 mM NaCl and 25 mM Tris–HCl (pH 7.5 at 25°C). After annealing, the DNA substrates were directly used in the smFRET measurements without further purification. Only those DNA constructs with two observable dyes (Cy3 and Cy5) were analyzed. For MT assays, the DNA substrate was constructed as previously described (29).

Single-molecule assay with magnetic tweezers

A flow chamber was assembled with two coverslips placed on an inverted microscope (IX71, Olympus, Japan). The coverslips were cleaned and modified with anti-digoxigenin protein. A magnetic bead was tethered to the modified coverslips through a single DNA substrate. An external magnetic force was applied to the magnetic bead by placing a permanent magnet above the chamber. DNA extension was monitored by analyzing the shape of the magnetic bead’s diffraction rings (30), which depended on the distance between the bead and the focal plane of the objective (100×, NA 1.45, Olympus). A stack of calibration images that recorded the shape of the diffraction rings versus distance was obtained by stepping the focal plane through a series of positions. After confirming the ssDNA–magnetic bead connections, the Pif1 helicase was added to the chamber. The Pif1 reaction buffer contained 50 mM NaCl, 1 mM MgCl₂, and 2 mM dithiothreitol (DTT) in 25 mM Tris–HCl (pH 7.5).

In the experiments to determine dependency on salt concentration, reaction buffers with 50, 100, 150 and 200 mM NaCl were used. DNA-unwinding events were monitored by recording the magnetic bead–surface distance, that is, the DNA extension, as a function of time. The time resolution was 30 ms. Changes in the DNA extension at a certain force and salt concentration were converted to the number of base pairs unwound by using the force–extension curve of ssDNA, as described by the freely jointed chain model (31). The effects of salt have been taken into account in the conversion between physical length (in nanometer) and number of base pairs (32). The average unwinding and translocation rates were calculated by the length of uninterrupted trace segments divided by the corresponding time duration.

Force calibration in the MT measurements was performed in two steps (33,34). Firstly, a force calibration curve $F(x)$, where x is the position of the magnet, was obtained. The pulling forces at more than ten positions of the magnet were measured for a 7-kb dsDNA connected to a magnetic bead. The $F(x)$ curves in Supplementary Figure S3A acquired from different DNA-bead complexes can be rescaled to overlap very well with each other by minimizing the mean square deviations from the averages (Supplementary Figure S3B). The rescaling process reflects the fact that the

force exerted on a bead is proportional to its saturated magnetic dipole moment. The rescaled data can be fitted to a double-exponential function, $F(x) = C \cdot [\exp(-x/k_1) + A \cdot \exp(-x/k_2)]$ (Supplementary Figure S3A and B). The next challenge is to quantitatively normalize the differences in force across the beads. We used the DNA hairpin in our MT assay as an internal force sensor. The critical force, at which the hairpin has equal probability to unzip and rezip, depends only on the thermodynamic and kinetic properties of the hairpin. In our experiments, the critical force is $F_c = 13.9 \pm 0.2$ pN measured by averaging over 20 magnetic beads, agreeing well with that reported for hairpins with random sequences (35,36). Before each unwinding measurement, we firstly tuned the magnet to a specific position $x_{1/2}$, at which the zipping and unzipping states of the hairpin are equally populated. The force at position x is then given by $F_c \cdot [F(x)/F(x_{1/2})]$. In such a way, the relative error of force can be constrained to within 3%.

Single-molecule fluorescence data acquisition and analyses

The smFRET study was carried out using an in-house-constructed objective-type total internal reflection fluorescence microscopy (37). Cy3 was excited with a 532 nm sapphire laser (Coherent Inc., Santa Clara, CA, USA). An oil immersion objective (100 \times , NA 1.49) was used to generate an evanescent field of illumination. The fluorescence signals from Cy3 and Cy5 were split using a dichroic mirror and finally collected using an electron-multiplying charge-coupled device camera (iXON; Andor Technology, South Windsor, CT, USA). The fluorescence imaging process was controlled and recorded using MetaMorph (Molecular Devices, San Jose, CA, USA). The coverslips (Thermo Fisher Scientific, USA) and slides were cleaned thoroughly by rinsing with acetone, methanol, a mixture of sulfuric acid and hydrogen peroxide (7:3, v/v), and sodium ethoxide. The surfaces of the coverslips were coated with a mixture of 99% methoxy-polyethylene glycol (PEG)-5000 (mPEG; Laysan Bio, Inc., Arab, AL, USA) and 1% biotin-PEG-5000 (Laysan Bio, Inc.). Streptavidin was added to the microfluidic chamber made of the PEG-coated coverslips and incubated for 5 min. After washing with buffer, ~ 100 pM DNA was added to the chamber and immobilized for 5 min. Free DNA molecules were removed by washing the chamber. Then, the chamber was filled with a reaction buffer containing 25 mM Tris-HCl (pH 8.0), 50 mM NaCl, 1 mM MgCl₂ and 2 mM DTT. During imaging, an oxygen-scavenging system containing 0.8% (w/w) D-glucose, 1 mg/ml of glucose oxidase (266.6 units/mg; Sigma-Aldrich, St. Louis, MO, USA), 0.4 mg/ml of catalase (2000–5000 units/mg; Sigma-Aldrich), and 1 mM Trolox was added to the Pif1 reaction buffer (37). An exposure time of 150 ms was used to record FRET signals before and after the Pif1 helicase (2 nM) was flowed into the chamber. All FRET assays were carried out at a constant temperature of 25°C. After correcting the local background, cross-talk, quantum yield and detection efficiency, the FRET efficiency was calculated (37). Finally, an unbiased step-finding algorithm was used to identify the binding ‘on’ and ‘off’ cases in the traces (38–42).

Modeling of exposed nucleotides at the 5'-end of co-crystallized ssDNA

In the crystal structures of ScPif1 (PDB ID: 5O6D) and BsPif1 (PDB ID: 5FTE), six deoxythymidine nucleotides in the form of an ssDNA fit into the cavity between domains 1A and 2A. Without altering the conformation of the co-crystallized ssDNA, nine additional deoxythymidine (dT) residues were added to the 5'-end. The extended ssDNA segment extrudes from the helicase and does not have contacts with the helicase to avoid model bias in the subsequent molecular dynamic simulations. Following the same protocol, the Pif1-DNA complexes with longer ssDNA chains were constructed by adding 12 and 15 dTs to the co-crystallized ssDNA, and control simulations were carried out to inspect the influence of DNA length on the dynamics of Pif1-DNA systems.

Molecular dynamics simulations and analysis

GROMACS version 5.1.2 was used to carry out MD simulations. CHARMM27 force fields were used to model both protein and DNA (43). Adenosine diphosphate (ADP) and ATP topologies were generated using the SWISSPARAM server (44). Complexes were enclosed in a triclinic box with the minimum distance from complex to box boundary set to 12 Å. The boxes were filled with TIP3P water molecules, and the systems were neutralized by adding Na⁺ and Cl⁻ ions at the desired concentration (50 or 200 mM). All systems were subjected to the steepest-descent energy minimization, after which they were visually inspected for structural deformities. Constant volume (NVT) and constant pressure (NPT) equilibrations were carried out for 1 and 2 ns step-wise at room temperature (300 K). During system equilibration, positional restraints were applied on heavy atoms. Temperature (300 K) and pressure (1 atmospheric pressure) were controlled by the V-rescale (45) and Parrinello–Rahman (46) methods, respectively. After NPT equilibration, the systems were propagated to 500 ns simulation trajectories. During production simulations, positional restraints were removed. For non-equilibrium pulling simulations, a stretching force was applied to the two terminal atoms of ssDNA, i.e. the C5' atom of the first nucleotide in the 5'-direction and the C3' atom of the last nucleotide. Each simulation with stretching forces on ssDNA was performed for 100 ns, starting with the converged structures obtained in equilibrium simulations. Throughout pulling simulations, constant forces were maintained at specified values (5–30 pN). The control simulations for complexes with longer ssDNA chains were carried out for 100 ns under 50 mM salt concentrations. Considering the increased computational cost, simulations with 200 mM salt or under pulling forces were carried out only on the Pif1-DNA complex with 15-nt ssDNA (6 co-crystallized dT's and 9 dT's from *in silico* modeling).

The molecular mechanics energy between the ssDNA and two helicases were calculated using the *gmx energy* command. This energy includes short-range coulombic and Lennard–Jones interaction terms between ssDNA and Pif1 helicases. The close contacts between helicase residues and the ssDNA were extracted from simulated structures for

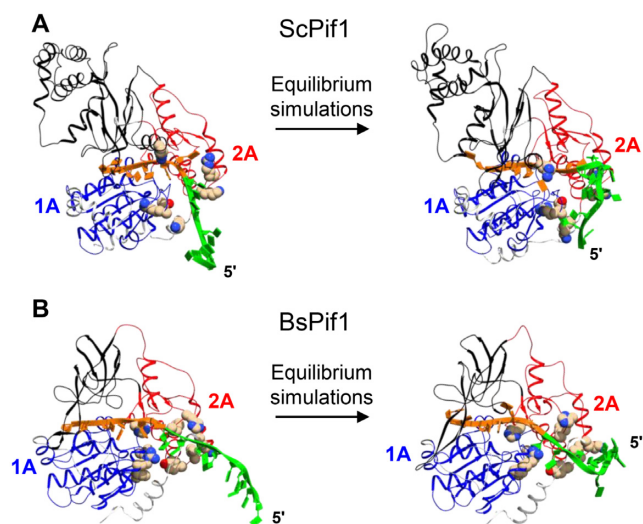


Figure 1. Binding conformations of ssDNA on Pif1 revealed in the MD simulations. (A) The initial model of the ssDNA–ScPif1 complex with 9 nt (green ribbon) extended from the 5′-end of the 6 nt segment (orange ribbon) co-crystallized with ScPif1 (left). After simulation, the ssDNA adopts a curved conformation, forming contacts to ScPif1 (right). (B) Result for BsPif1, as described in (A). Domain color: blue for 1A; red for 2A. The amino acids interacting with the ssDNA are shown as van der Waals spheres (yellow for carbon atoms; blue for nitrogen atoms; red for oxygen atoms, hydrogen atoms are not shown for clarity purposes).

any two residues from each group within 3.0 Å. The contacting occupancy is based on the statistics from the structure samples in the last 50 ns of the simulation trajectories. The end-to-end distances of ssDNA was calculated using the *gmx distance* between the C5′ and C3′ atoms of the nucleotides at the 5′- and 3′-ends, respectively. Electrostatic potential maps were computed using the adaptive Poisson–Boltzmann solver (APBS) method (47) with default parameters, and the model figures were prepared using UCSF Chimera (48).

RESULTS

Molecular dynamics (MD) simulations of ssDNA–helicase interactions

We first built atomic models with adjacent nucleotides based on high-resolution crystal structures to investigate the ssDNA interactions with the two Pif1 helicases. Because only six nucleotides that are fully bound by the helicases are resolved in the high-resolution crystal structures, adjacent segment of ssDNA was constructed prior to molecular dynamics simulations. The nucleotides co-crystallized with ScPif1 or BsPif1 in their crystal structures (5O6D for ScPif1 and 5FTE for BsPif1; Supplementary Figure S1D and E) were kept intact, and a 9-nucleotide long ssDNA segment was added to the DNA at the 5′-end in each system. The ssDNA was modeled to ensure that the extended ssDNA segment extruded from the surfaces of the helicases such that the model bias in ssDNA–helicase interactions was small (Figure 1A and B, left). After the ssDNA extension modeling, all-atom molecular dynamics (MD) simulations of the helicase–DNA complexes were carried out

under equilibrium conditions at 300 K and 1 atmospheric pressure. Through the simulations, the helicases and the co-crystallized ssDNA were stable, but the extended ssDNA segment that was exposed to solvent exhibited large conformational changes and gradually formed contacts with the helicases (Supplementary Movies S1 and S2). The exposed ssDNA segment interacts with the 2A domain and adopts a curved path on the protein surface (Figure 1A and B, right, Supplementary Figures S4 and S5). For ScPif1, the interactions are dominantly between negatively charged nucleotides and positively charged protein residues on the surface of the 2A domain near the 5′-ssDNA. For BsPif1, the electrostatic and van der Waals interactions both are important for ssDNA–helicase binding. The interactions of the Pif1 helicases with the exposed ssDNA are not highly specific, but rather dynamical, in contrast to the interactions between Pif1 and co-crystallized ssDNA segment (see Supplementary Figures S4 and S5). The occupancy of major contacts shown in Supplementary Figure S6 also reflects their dynamical nature.

Focusing on the exposed ssDNA segment, the interacting residues are mainly lysine and arginine in ScPif1, while the DNA-interacting amino acids of BsPif1 are composed of both basic and hydrophobic residues (Supplementary Figures S6 and S7). We also observed aromatic residues (phenylalanine and tyrosine) forming frequent contacts with the ssDNA in the BsPif1–DNA complex simulation. The 6 nt co-crystallized ssDNA segment buried in ScPif1 and BsPif1 is in a nearly straight conformation (Figure 1A and B, orange) with average end-to-end distances (L_{1-6}) of 2.8 nm and 2.7 nm, respectively (Supplementary Figure S8A and B). In contrast, the end-to-end distances of the 15 nt ssDNA, including the simulation-reconstructed 9 nt segments, are 3.9 nm in ScPif1 and 5.2 nm in BsPif1 (Supplementary Figure S8A and B) because of the curved conformations of the ssDNA in the two helicases. It is noteworthy that the ssDNA exhibited structural diversity that was observed from independent simulations, consistent with the dynamical nature of the exposed ssDNA (Supplementary Figure S4C and D). Nonetheless, the ssDNA in all simulations was consistently converged to curved conformations when bound to helicases. In these simulations, we did not observe significant changes in the RecA positioning with respect to the ssDNA. Furthermore, the Pif1–DNA complexes with longer ssDNA chains were constructed by adding 12 or 15 nucleotides to the co-crystallized DNA. MD simulations of these systems reveal consistent trends as observed in the case of 9-dT exposed ssDNA (Supplementary Figure S9). The exposed ssDNA quickly forms curved conformations and establishes contacts with Pif1 helicases, suggesting that the present results are valid in the presence of longer ssDNA.

smFRET assay of ssDNA binding to the helicases

As an emerging technique for studying structural dynamics (7,49), smFRET was applied to measure the distances between dye-labeled sites. We adopted a DNA nanotensioner recently designed by our group (42) to study the conformational changes of ssDNA in complex with a helicase (Figure 2A and B, left). In the DNA nanotensioner, a double-

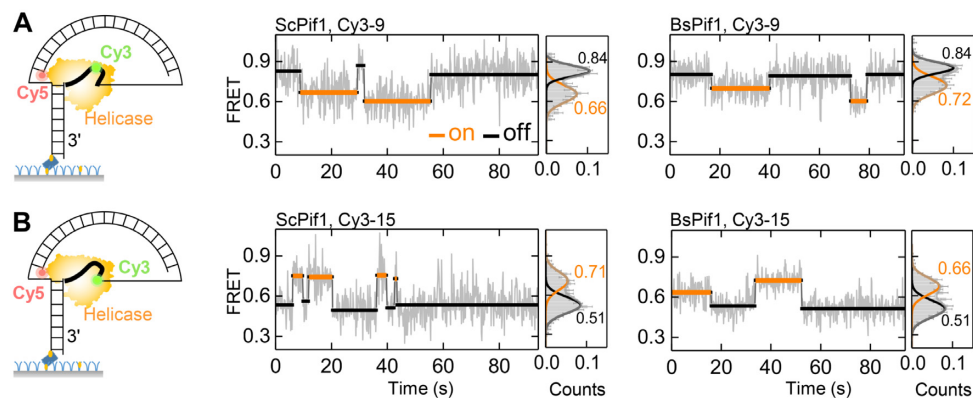


Figure 2. Binding assay of ssDNA onto Pif1 at 50 mM NaCl with smFRET. DNA nanotensioners were used to enhance the precision of the smFRET. Cy3 was labeled at the 9th (A) or 15th (B) nucleotide of the 5'-tail. Yellow lines and black lines in the FRET traces represent the Pif1 binding 'on' and 'off' states, respectively. The histogram for each 'on' or 'off' case was built from 220 events. Error bars on the histograms represent the statistical error in the bins.

stranded DNA (dsDNA) was bent to exert a tension of ~ 6 pN on the 30-nt 5'-loading tail of a DNA hairpin that is the substrate of Pif1 (42). The design of the nanotensioner was inspired by the D-loop structure of DNA during homologous recombination for break-induced DNA replication, which engages Pif1 (19). The tension exerted on the ssDNA overhang reduces its fluctuations so that the smFRET becomes more sensitive to the protein-induced conformational changes than that of the freely fluctuating overhang of a simple DNA hairpin. The ssDNA conformation was characterized by two feature distances using two specially designed constructs: a nucleotide at the 9th or 15th position from the fork of the DNA hairpin in the 5'-direction was labeled with a Cy3 dye as a fluorescence donor (denoted as Cy3-9 or Cy3-15), while the acceptor Cy5 was labeled on the 3'-side of the fork (Supplementary Figure S2 and Supplementary Table S2). The ssDNA was straightened prior to Pif1-hairpin fork binding via the tension generated by the bent dsDNA. The distance between the two dyes (Cy3 and Cy5; Förster distance = ~ 5.8 nm) is set by the tension. Without protein binding, the average position of Cy5 is located farther from Cy3-15 than from Cy3-9 by ~ 1.9 nm (Supplementary Figure S10) (50), indicating a straight conformation under the tension (~ 6 pN) exerted by the DNA nanotensioner (42,50). Upon adding ScPif1, two states were observed in the FRET time traces: a binding 'on' state marked with yellow lines and a binding 'off' state marked with black lines (Figure 2A and B, middle). The segments of the binding 'on' and 'off' states were identified by an unbiased step-finding algorithm (38–42). The FRET efficiencies of the binding 'on' or 'off' states were quantified by computing their histograms from the corresponding time traces. From these histograms, FRET efficiencies of the binding 'on' state corresponding to the histogram peaks are 0.66 for Cy3-9 and 0.71 for Cy3-15 (Figure 2A and B, middle). The difference between the two FRET efficiencies is ~ 0.05 , corresponding to a distance difference of ~ 0.2 nm, with Cy3-15 being even closer to Cy5 than Cy3-9. This can be explained by the curved conformation of ssDNA induced by ScPif1, as observed in our MD simulations, where the exposed ssDNA segment (7–15 nt) bound onto ScPif1. Using the same approach, we analyzed the ssDNA conformation

upon BsPif1 binding (Figure 2A and B, right). In this case, the difference of the binding 'on' state in the two FRET peaking signals (histograms in Figure 2A and B, right) is -0.06 , indicating that Cy3-15 is ~ 0.2 nm farther away from Cy5 than Cy3-9. Although the 15th nucleotide is located farther away from the Cy5 dye, the 0.2 nm distance difference is not sufficient to account for a 6-nt ssDNA segment with a distance of ~ 1.9 nm at ~ 6 pN. Therefore, the results suggest that ssDNA is also curved when bound to BsPif1, although at a less curved level compared with the case of ScPif1 binding. We estimated the positions of Cy5 according to the ssDNA conformations given by the MD simulations and the Cy3–Cy5 distances measured with smFRET (Supplementary Figure S8). We attempted to dock a dsDNA to each of the structures to rationalize our calculations (Supplementary Figure S8C and D). It is noteworthy that the positions and orientations of the dsDNA should be considered just as a guidance because we are not able to determine them uniquely based on the given restraints (cf. Supplementary Figure S1A–C).

We performed smFRET measurements in both 50 and 200 mM NaCl buffers. The protein binding-induced changes in FRET were significant in both cases (Figure 2, Supplementary Figure S11). Interestingly, we observed a new peak at FRET ≈ 0.43 for ScPif1 in the 200 mM NaCl buffer, which means that a few nucleotides of the curved ssDNA adjacent to the 6-nt segment may dissociate from the helicase in the high salt concentration buffer. We posit that the high salt concentration may also weaken the binding of the helicase to its substrate. Indeed, we found that the binding time of ScPif1 reduces from 2.0 ± 0.2 s in the 50 mM NaCl buffer to 1.4 ± 0.1 s in the 200 mM NaCl buffer (Supplementary Figure S12).

Force regulation of DNA unwinding and translocation of the helicases

We designed MD simulations with stretching forces on ssDNA to assess the stability of ssDNA–helicase binding under the influence of external forces. Based on the converged structures observed in the equilibrium-state simulations, with the ssDNA bound to the helicase, as the start-

ing model, we performed MD simulations under stretching forces exerted on two ends of the ssDNA. Constant forces were simulated by attaching the two ends of the ssDNA on springs, with the forces pulling in opposite directions to stretch the ssDNA. Simulation data showed that the ssDNA remained bound to the helicases when the stretching forces were small in both systems, reflected in the small fluctuations of end-to-end distances around constant values (Figure 3). Under larger forces (≥ 30 pN for ScPif1 and ≥ 20 pN for BsPif1), the ssDNA became straightened, as indicated by its increased end-to-end distances. As the ssDNA was straightened, the exposed ssDNA segment dissociated from the helicases, losing its contacts with the surface of helicases (Figure 3, Supplementary Movies S3 and S4).

We performed MT experiments to monitor the DNA-unwinding activities of the two helicases under various force strengths (Figure 4A and Supplementary Table S3). DNA unwinding was observed after the helicase (5 nM) and ATP (2 mM) were added into the flow chamber. No unwinding signals could be observed if ATP was replaced by ADP (Supplementary Figure S13). Typical unwinding traces are displayed in Supplementary Figure S14, revealing sawtooth patterns with short unwinding bursts (51). Representative bursts are displayed in the top panels of Figure 4B and C to illustrate that the unwinding (colored in black) is interrupted by pauses (colored in pink) and back-slidings (large jumps in measured DNA length, colored in blue) on the tracking strand, accompanied by translocations (gradually reduction in DNA length, colored in orange) or slidings (colored in blue) on the displaced strand. The unwinding and translocation rates at the uninterrupted trace segments were analyzed (Supplementary Figure S14 and S15) (52). The unwinding rate is slightly lower than the translocation rate (Figure 4B and C, bottom), because a helicase should break the base pairs during dsDNA unwinding, which is not required for ssDNA translocation (53–58).

The DNA-unwinding and translocation rates of ScPif1 are not sensitive to the forces below 10 pN. The rates are in agreement with that measured with smFRET at zero force (Supplementary Figure S16 and S17) and those reported in the literature (59,60). When the force is larger than 10 pN, there is a substantial drop in both unwinding and translocation rates (Figure 4B, bottom). The unwinding time, which is inversely proportional to the dissociation rate of the protein from its substrate (61), is also significantly reduced (Supplementary Figure S14). This phenomenon suggested that forces beyond a critical value hinder ScPif1 function. Specifically, for ScPif1 at 13 pN force, the unwinding and translocation rates both reduce to about 40% of the rates observed at 10 pN. The DNA hairpin would be unzipped at forces larger than 13 pN (Supplementary Figure S3). The reduced activity can be attributed to the weakening of the ssDNA–Pif1 interactions when the exposed ssDNA dissociates from the helicase surface under large forces. The force has smaller effects on the BsPif1 activity than on the ScPif1 activity (Figure 4C, bottom). The unwinding and translocation rates for BsPif1 at 13 pN only reduce to ~ 80 – 90% of the highest rates observed at 10 pN.

The critical strengths of forces that result in ssDNA dissociation from the two helicases was ~ 20 – 30 pN in the MD simulations, while in the MT experiments, the measured

forces were only 10 pN. The difference in the forces between these two methods is related to the difference in timescales in the pulling execution (62), which were ~ 100 ns in the MD simulations and ~ 1 s in the MT experiments, respectively. Specifically for ScPif1, the lifetime of the ssDNA bound state follows $\tau(f) = \tau(0) \exp(-f \Delta x / k_B T)$, where $\tau(0)$ is the lifetime at zero force, Δx is the distance applied by f , k_B is the Boltzmann constant, and T is temperature (62). Knowing that the lifetime of the ssDNA–helicase interaction was ~ 100 ns and $\Delta x \approx 2.8$ nm at 30 pN in the MD simulations (Figure 3), the lifetime at 10 pN was estimated to be of the order of 1 s. In this aspect, the MD simulation results were consistent with those of the MT experiments.

Salt concentration regulation of enzymatic activities of helicases

For ScPif1, the electrostatic potential surface calculated from the complex structures revealed large, positively charged patches on the 2A domain surface (Figure 5A), which was further confirmed by amino acid compositional analysis (63). Because these positively charged patches are located near the 5'-end of ssDNA, they are highly likely to form favorable interactions with negatively charged nucleotides. Following this observation, we propose that salt concentration is an influential factor of helicase activities. This hypothesis was tested by MT experiments described in the following. The unwinding and translocation rates of ScPif1 or BsPif1 at different NaCl concentrations within a range of physiological relevance were measured (Figure 5C and D and Supplementary Figure S18). The unwinding and translocation rates of ScPif1 monotonically reduced by about 19% as the NaCl concentration was increased (Figure 5C). The negative correlation between helicase activity and NaCl concentration suggested that the DNA–helicase interactions are weaker at higher salt concentrations, which is in accordance with electrostatic screening effects (64,65).

We also compared the ssDNA–helicase interactions at two NaCl concentrations (50 mM versus 200 mM) using MD simulations and calculated the interaction energies between the exposed ssDNA and the two helicases. The ssDNA showed weaker interactions with ScPif1 at 200 mM NaCl concentration than the case of 50 mM salt concentration (Table 1). Consistently, the exposed ssDNA exhibited larger conformational fluctuations (Supplementary Figure S19A). These results suggest that the reduced activity of ScPif1 at increased salt concentrations is due to stronger electrostatic screening effects on the ssDNA–helicase interactions (27,66). In the case of BsPif1, the change in NaCl concentration had a less pronounced effect on the unwinding and translocation rates (Figure 5D), which is consistent with the observation that ssDNA–BsPif1 electrostatic interactions are less dominant than ssDNA–ScPif1 electrostatic interactions (Figure 5B).

There were five positively charged residues of ScPif1 (R391, R502, R750, K752, K756) and only two positively charged residues of BsPif1 (R155, K405) that formed contacts with the exposed ssDNA revealed in the MD simulations at 50 mM NaCl concentration (Supplementary Figure S6). The ssDNA–BsPif1 physical interactions (composed

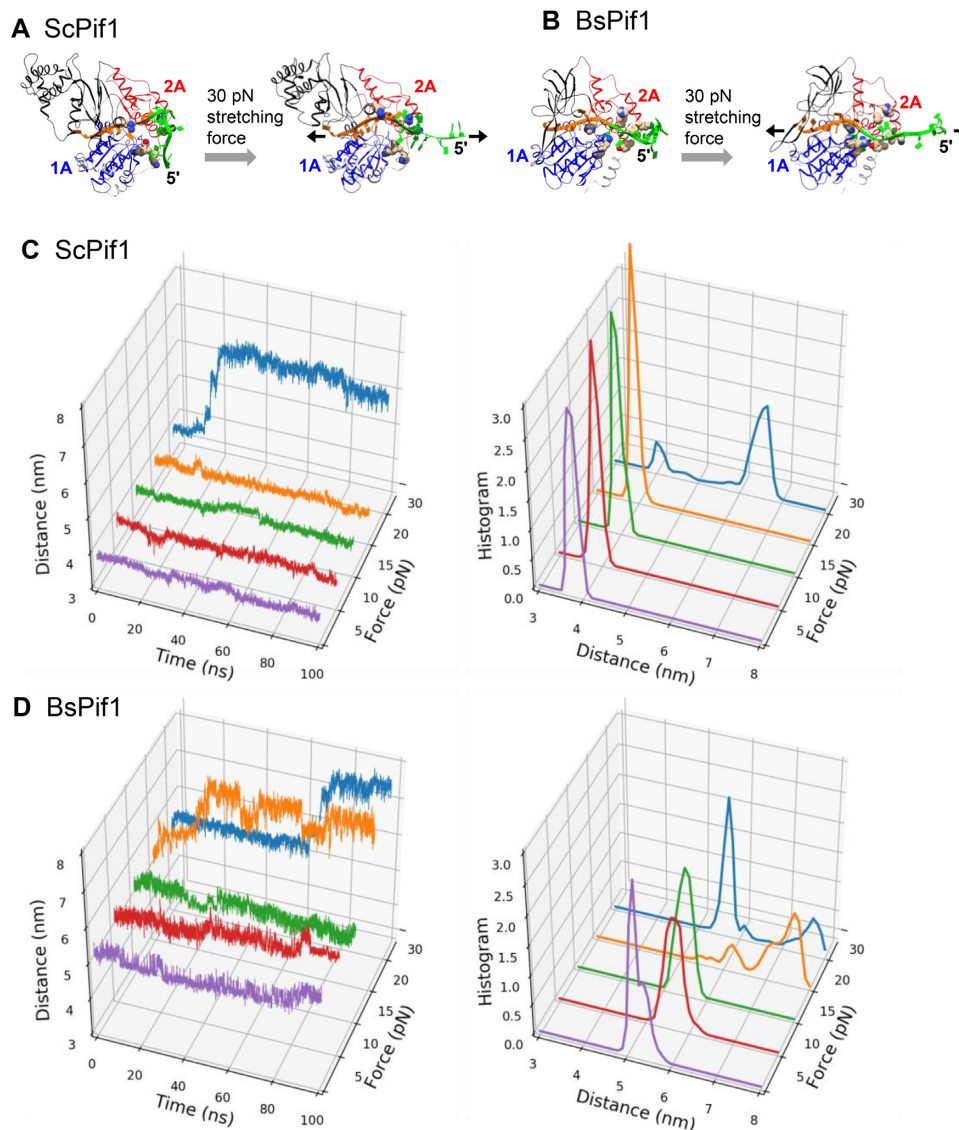


Figure 3. End-to-end distances of ssDNA in complex with Pif1 under different stretching forces revealed in MD simulations. (A, B) MD simulation results of ssDNA being pulled off from ScPif1 or BsPif1 by a stretching force. (C) Time traces of the DNA end-to-end distance under various forces (left). When the force is sufficiently large, the exposed segment of the ssDNA is pulled off from ScPif1 (sudden increase in length at 30 pN). Length distribution of each trace at each force (right). (D) Same information for ssDNA bound to BsPif1. The relative longer length of ssDNA in BsPif1 indicates a less curved conformation than the ssDNA bound to ScPif1, which is in accordance with the smFRET results. The stretching forces are exerted on the two terminal atoms (C5' and C3') of the ssDNA backbone.

of electrostatic and Lennard–Jones terms) are less sensitive to the change in NaCl concentration than the ssDNA–ScPif1 physical interactions (Table 1). The conformation and dynamics of the exposed ssDNA segment are similar for ssDNA–BsPif1 complex at both NaCl concentrations (Supplementary Figure S19B). In the ssDNA–ScPif1 complex, the positively charged patch of ScPif1 observed from the MD simulations suggests that ScPif1 utilizes the electrostatic interactions to facilitate DNA unwinding. At 200 mM NaCl concentration, the interactions between the exposed nucleotides and charged residues reduce significantly, weakening ssDNA–ScPif1 binding. The reduced interactions can be a source of slower unwinding and translocation observed at the single-molecule level.

DISCUSSION

The conformation of ssDNA in the DNA–helicase complexes is crucial for their enzymatic activities (23,24,67). However, because of the dynamic characteristics of the ssDNA that moves in solution or partially binds to the helicase surface, it is challenging to obtain the high-resolution crystal structure of the ssDNA using conventional structure determination methods. The DNA conformational flexibility also presents a challenge for structure determination by electron microscopy. The lack of structures for such flexible but functionally critical regions may yield incomplete or sometimes incorrect understanding of the underlying molecular mechanisms. In this study, by combining single-molecule techniques with all-atom structure model-

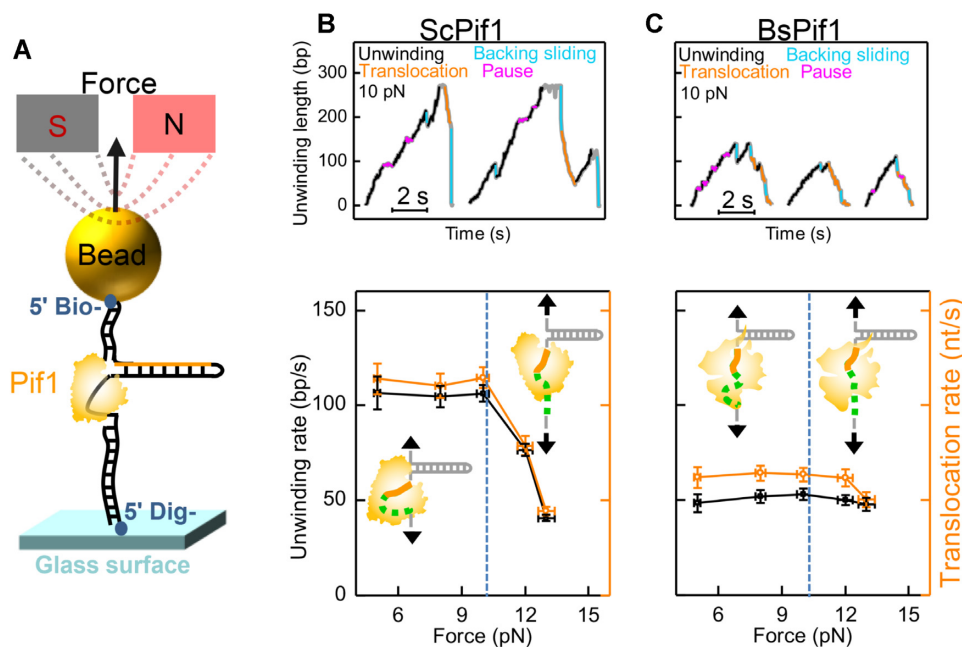


Figure 4. Force-induced regulation of DNA unwinding and translocation of Pif1. (A) Sketch of the MT experiment. (B) Typical DNA-unwinding bursts of ScPif1 at 10 pN (top) and average unwinding and translocation rates under various forces (bottom). (C) Experimental results for BsPif1, as described in (B). The error bars are the standard error of the mean (SEM). Insets: Models of DNA–Pif1 complex under small or large forces; the arrows represent the stretching force. The number of trace segments analyzed was 150–200.

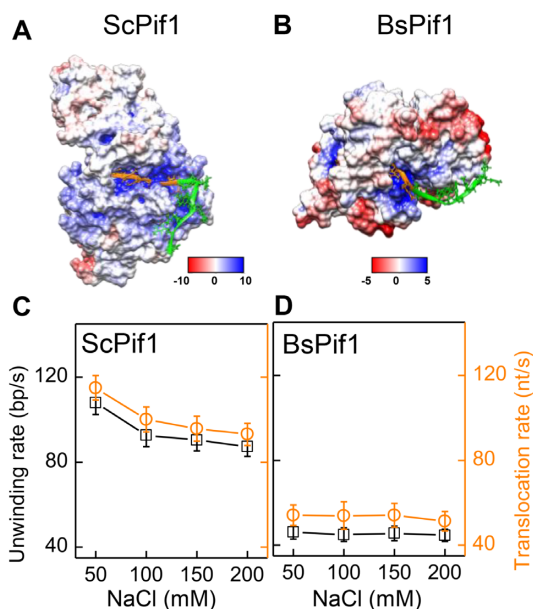


Figure 5. Salt-induced regulation of the unwinding and translocation of Pif1 at 8 pN. (A, B) Electrostatic potential surface maps of ScPif1 (A) and BsPif1 (B) at 50 mM NaCl according to simulation, with colors from blue (positive) to red (negative) in the unit of $k_B T/e$. (C, D) Salt dependences of the DNA-unwinding rate and the translocation rate of ScPif1 (C) and BsPif1 (D). Error bars indicate the SEM. The number of trace segments analyzed was 150–200.

ing and MD simulations, we identified plausible conformations of ssDNA in ssDNA–helicase complexes that cannot be determined by conventional methods. Two Pif1 helicases,

Table 1. Calculated interaction energy and contacts between the nine exposed nucleotides and Pif1

Helicase	[NaCl]	Interaction energy ^a (kcal/mol)	Number of atom contacts ^b
ScPif1	50 mM NaCl	-205 ± 16	103 ± 11
	200 mM NaCl	-161 ± 20	80 ± 15
BsPif1	50 mM NaCl	-187 ± 12	128 ± 12
	200 mM NaCl	-182 ± 12	132 ± 13

^aThe interaction includes the electrostatic and van der Waals terms.

^bAtom pairs with interatomic distance within 3.0 Å.

namely, a eukaryotic ScPif1 and a prokaryotic BsPif1, were studied. By combining the above mentioned methods, we identified ssDNA segments adjacent to the bound DNA form close contacts with the RecA-like domains (1A and 2A) of the helicases, which is essential for the inch-worm mechanism in which the helicases move along ssDNA by alternating affinities between the two RecA-like domains and the ssDNA. The roles of the exposed ssDNA on the enzymatic activities of the helicases were systematically analyzed by the MT experiments, revealing that both force and salt concentration may regulate the unwinding and translocation of the helicases.

We used Poly(dT) to model the exposed regions of ssDNA, which followed the Poly(dT) resolved in the Pif1 crystal structures. Here, our primary goal is to investigate the interactions between the flexible ssDNA and the positively charged regions on the helicases. Since the nucleotides carry negative charges mainly originating from their backbones, the nucleotide composition is less crucial in this study. By varying the length of exposed ssDNA segment, we argue

that the extended ssDNA composed of 9 nt is sufficient to study the conformational flexibility and to reveal the interactions between ssDNA and the helicases. A closer examination on the electrostatic potential surface of the two helicases reveals that an ssDNA segment of 9 nt can cover the positively charged patches. Simulations with longer exposed segments can reveal richer dynamics, but at the cost of more computing time. Since the general trends revealed by the systems with 9-nt exposed ssDNA were validated with the longer ssDNA, we employ the models with 9-nt exposed ssDNA to investigate the salt concentration or stretching force dependent dynamics.

In this study, MD simulations demonstrated their power in two aspects. First, the simulations generated detailed structural models for the exposed ssDNA, which is difficult to investigate using experimental approaches. These modeling and simulations revealed that ssDNA binds to helicases and forms curved conformations, which were then validated using smFRET experiments. Second, the simulations provided the molecular mechanisms underlying the force and salt regulation of helicase activity. The stretching force on ssDNA exerted using MTs was mimicked by applying simulated forces to the two ends of the ssDNA. Large stretching forces result in partial or full dissociation of the ssDNA from the helicase, explaining the reduction in enzymatic activity. The salt screening effects were analyzed by quantitatively comparing the ssDNA–helicase interactions at 50 and 200 mM NaCl concentrations. As expected, electrostatic interactions become weaker in 200 mM NaCl solution compared to those in 50 mM NaCl solution. Salt affects the ScPif1 activity more significantly than the BsPif1 activity as electrostatic interactions are more crucial for ScPif1. The structure–function correlation highlights the key roles of the dynamic ssDNA–helicase interactions. Conformational fluctuations can be found in many helicases, such as PcrA (Supplementary Figure S1A), BLM (Supplementary Figure S1B and C) (10,15,16) and those listed in Supplementary Table S1. The synergetic approach, by combining single-molecule techniques and computational modeling/simulations, is applicable to biomolecular systems in obtaining information about structure–function relationships that is not immediately accessible by current structure determination methods.

DATA AVAILABILITY

All relevant data are included in the manuscript and the Supplementary Data file. Any other data are available from the authors on request.

SUPPLEMENTARY DATA

Supplementary Data are available at NAR Online.

ACKNOWLEDGEMENTS

We thank Dr. Zakian for providing the plasmid encoding yeast Pif1 gene.

Author contributions: J.L. and J.M. performed the experiments. V.K. and H.L. performed molecular dynamics simulations. C.X. constructed the DNA substrates. X.X. pro-

duced the proteins. M.L., Y.L., H.L., J.L., J.M., H.F., X.H., S.W., Q.J. and Q.F. analyzed the data and wrote the paper.

FUNDING

National Natural Science Foundation of China [12090051, 11834018, 91753104, U1930402, 12090050]; Strategic Priority Research Program of the Chinese Academy of Sciences [XDB37000000]; National Key Research and Development Program of China [2019YFA0709304]; CAS Key Research Program of Frontier Sciences [ZDBS-LY-SLH015]; Y.L. is supported by the Youth Innovation Promotion Association of CAS [Y2021003]; Tianhe-2JK computing time award at the Beijing Computational Research Center (CSRC). Funding for open access charge: National Natural Science Foundation of China [12022409].

Conflict of interest statement. None declared.

REFERENCES

- Fairman-Williams, M.E., Guenther, U.P. and Jankowsky, E. (2010) SF1 and SF2 helicases: family matters. *Curr. Opin. Struct. Biol.*, **20**, 313–324.
- Pyle, A.M. (2008) Translocation and unwinding mechanisms of RNA and DNA helicases. *Annu. Rev. Biophys.*, **37**, 317–336.
- Caruthers, J.M. and McKay, D.B. (2002) Helicase structure and mechanism. *Curr. Opin. Struct. Biol.*, **12**, 123–133.
- Vindigni, A. (2007) Biochemical, biophysical, and proteomic approaches to study DNA helicases. *Mol. Biosyst.*, **3**, 266–274.
- Crickard, J.B. and Greene, E.C. (2019) Helicase mechanisms during homologous recombination in *saccharomyces cerevisiae*. *Annu. Rev. Biophys.*, **48**, 255–273.
- Vindigni, A. and Hickson, I.D. (2009) RecQ helicases: multiple structures for multiple functions? *HFSP J.*, **3**, 153–164.
- Lerner, E., Cordes, T., Ingargiola, A., Alhadid, Y., Chung, S., Michael, X. and Weiss, S. (2018) Toward dynamic structural biology: two decades of single-molecule Förster resonance energy transfer. *Science*, **359**, eaan1133.
- Lu, K.Y., Chen, W.F., Rety, S., Liu, N.N., Wu, W.Q., Dai, Y.X., Li, D., Ma, H.Y., Dou, S.X. and Xi, X.G. (2018) Insights into the structural and mechanistic basis of multifunctional *s. cerevisiae* pif1p helicase. *Nucleic Acids Res.*, **46**, 1486–1500.
- Chen, W.F., Dai, Y.X., Duan, X.L., Liu, N.N., Shi, W., Li, N., Li, M., Dou, S.X., Dong, Y.H., Rety, S. *et al.* (2016) Crystal structures of the Bspif1 helicase reveal that a major movement of the 2B SH3 domain is required for DNA unwinding. *Nucleic Acids Res.*, **44**, 2949–2961.
- Velankar, S.S., Soultanas, P., Dillingham, M.S., Subramanya, H.S. and Wigley, D.B. (1999) Crystal structures of complexes of PcrA DNA helicase with a DNA substrate indicate an inchworm mechanism. *Cell*, **97**, 75–84.
- Zhou, X., Ren, W., Bharath, S.R., Tang, X., He, Y., Chen, C., Liu, Z., Li, D. and Song, H. (2016) Structural and functional insights into the unwinding mechanism of *Bacteroides sp* Pif1. *Cell Rep.*, **14**, 2030–2039.
- Su, N., Byrd, A.K., Bharath, S.R., Yang, O., Jia, Y., Tang, X., Ha, T., Raney, K.D. and Song, H. (2019) Structural basis for DNA unwinding at forked dsDNA by two coordinating Pif1 helicases. *Nat. Commun.*, **10**, 5375.
- Lohman, T.M., Tomko, E.J. and Wu, C.G. (2008) Non-hexameric DNA helicases and translocases: mechanisms and regulation. *Nat. Rev. Mol. Cell Biol.*, **9**, 391–401.
- Dai, Y.X., Chen, W.F., Liu, N.N., Teng, F.Y., Guo, H.L., Hou, X.M., Dou, S.X., Rety, S. and Xi, X.G. (2021) Structural and functional studies of SF1B Pif1 from *thermus oshimai* reveal dimerization-induced helicase inhibition. *Nucleic Acids Res.*, **49**, 4129–4143.
- Swan, M.K., Legris, V., Tanner, A., Reaper, P.M., Vial, S., Bordas, R., Pollard, J.R., Charlton, P.A., Golec, J.M.C. and Bertrand, J.A. (2014) Structure of human Bloom's syndrome helicase in complex with ADP and duplex DNA. *Acta Crystallogr. D Biol. Crystallogr.*, **70**, 1465–1475.

16. Newman, J.A., Savitsky, P., Allerston, C.K., Bizard, A.H., Özer, Ö., Sarlós, K., Liu, Y., Pardon, E., Steyaert, J., Hickson, I.D. *et al.* (2015) Crystal structure of the Bloom's syndrome helicase indicates a role for the HRDC domain in conformational changes. *Nucleic Acids Res.*, **43**, 5221–5235.
17. Budd, M.E., Reis, C.C., Smith, S., Myung, K. and Campbell, J.L. (2006) Evidence suggesting that Pif1 helicase functions in DNA replication with the Dna2 helicase/nuclease and DNA polymerase δ . *Mol. Cell Biol.*, **26**, 2490–2500.
18. Pike, J.E., Henry, R.A., Burgers, P.M., Campbell, J.L. and Bambara, R.A. (2010) An alternative pathway for Okazaki fragment processing: resolution of fold-back flaps by Pif1 helicase. *J. Biol. Chem.*, **285**, 41712–41723.
19. Wilson, M.A., Kwon, Y.H., Xu, Y., Chung, W.H., Chi, P., Niu, H., Mayle, R., Chen, X., Malkova, A., Sung, P. *et al.* (2013) Pif1 helicase and Pol δ promote recombination-coupled DNA synthesis via bubble migration. *Nature*, **502**, 393–396.
20. Saini, N., Ramakrishnan, S., Elango, R., Ayyar, S., Zhang, Y., Deem, A., Ira, G., Haber, J.E., Lobachev, K.S. and Malkova, A. (2013) Migrating bubble during break-induced replication drives conservative DNA synthesis. *Nature*, **502**, 389–392.
21. Schulz, V.P. and Zakian, V.A. (1994) The *saccharomyces* PIF1 DNA helicase inhibits telomere elongation and de novo telomere formation. *Cell*, **76**, 145–155.
22. Zhou, J.-Q., Monson, E.K., Teng, S.-C., Schulz, V.P. and Zakian, V.A. (2000) Pif1p helicase, a catalytic inhibitor of telomerase in yeast. *Science*, **289**, 771–774.
23. Gu, Y., Wang, J., Li, S., Kamiya, K., Chen, X. and Zhou, P. (2013) Determination of the biochemical properties of full-length human PIF1 ATPase. *Prion*, **7**, 341–347.
24. George, T., Wen, Q., Griffiths, R., Ganesh, A., Meuth, M. and Sanders, C.M. (2009) Human Pif1 helicase unwinds synthetic DNA structures resembling stalled DNA replication forks. *Nucleic Acids Res.*, **37**, 6491–6502.
25. Curti, E., Smerdon, S.J. and Davis, E.O. (2007) Characterization of the helicase activity and substrate specificity of mycobacterium tuberculosis UvrD. *J. Bacteriol.*, **189**, 1542–1555.
26. Van Komen, S., Reddy, M.S., Krejci, L., Klein, H. and Sung, P. (2003) ATPase and DNA helicase activities of the *Saccharomyces cerevisiae* anti-recombinase Srs2. *J. Biol. Chem.*, **278**, 44331–44337.
27. Boulé, J.-B. and Zakian, V.A. (2007) The yeast pif1p DNA helicase preferentially unwinds RNA–DNA substrates. *Nucleic Acids Res.*, **35**, 5809–5818.
28. Liu, N.N., Duan, X.L., Ai, X., Yang, Y.T., Li, M., Dou, S.X., Retz, S., Deprez, E. and Xi, X.G. (2015) The *bacteroides* sp. 3_I_23 Pif1 protein is a multifunctional helicase. *Nucleic Acids Res.*, **43**, 8942–8954.
29. Wang, S., Qin, W., Li, J.H., Lu, Y., Lu, K.Y., Nong, D.G., Dou, S.X., Xu, C.H., Xi, X.G. and Li, M. (2015) Unwinding forward and sliding back: an intermittent unwinding mode of the BLM helicase. *Nucleic Acids Res.*, **43**, 3736–3746.
30. Strick, T.R., Allemand, J.F., Bensimon, D., Bensimon, A. and Croquette, V. (1996) The elasticity of a single supercoiled DNA molecule. *Science*, **271**, 1835–1837.
31. Smith, S.B., Cui, Y. and Bustamante, C. (1996) Overstretching B-DNA: the elastic response of individual double-stranded and single-stranded DNA molecules. *Science*, **271**, 795–799.
32. Bosco, A., Camunas-Soler, J. and Ritort, F. (2014) Elastic properties and secondary structure formation of single-stranded DNA at monovalent and divalent salt conditions. *Nucleic Acids Res.*, **42**, 2064–2074.
33. Shon, M.J., Rah, S.H. and Yoon, T.Y. (2019) Submicrometer elasticity of double-stranded DNA revealed by precision force-extension measurements with magnetic tweezers. *Sci. Adv.*, **5**, eaav1697.
34. Chen, H., Fu, H., Zhu, X., Cong, P., Nakamura, F. and Yan, J. (2011) Improved high-force magnetic tweezers for stretching and refolding of proteins and short DNA. *Biophys. J.*, **100**, 517–523.
35. Greenleaf, W.J., Frieda, K.L., Abbondanzieri, E.A., Woodside, M.T. and Block, S.M. (2007) High-resolution, single-molecule optical trapping measurements of transcription with basepair accuracy: instrumentation and methods. *Proc. of SPIE*, **6644**, 664406.
36. Woodside, M.T., Behnke-Parks, W.M., Larizadeh, K., Travers, K., Herschlag, D. and Block, S.M. (2006) Nanomechanical measurements of the sequence-dependent folding landscapes of single nucleic acid hairpins. *Proc. Natl. Acad. Sci. U.S.A.*, **103**, 6190–6195.
37. Roy, R., Hohng, S. and Ha, T. (2008) A practical guide to single-molecule FRET. *Nat. Methods*, **5**, 507–516.
38. Kerresmakers, J.W.J., Munteanu, E.L., Laan, L., Noetzel, T.L., Janson, M.E. and Dogterom, M. (2006) Assembly dynamics of microtubules at molecular resolution. *Nature*, **442**, 709–712.
39. Myong, S., Bruno, M.M., Pyle, A.M. and Ha, T. (2007) Spring-loaded mechanism of DNA unwinding by hepatitis C virus NS3 helicase. *Science*, **317**, 513–516.
40. Blosser, T.R., Yang, J.G., Stone, M.D., Narlikar, G.J. and Zhuang, X. (2009) Dynamics of nucleosome remodelling by individual ACF complexes. *Nature*, **462**, 1022–1027.
41. Ma, J., Chen, Z., Xu, C., Huang, X., Jia, Q., Zou, Z., Mi, C., Ma, D., Lu, Y., Zhang, H. *et al.* (2020) Dynamic structural insights into the molecular mechanism of DNA unwinding by the bacteriophage T7 helicase. *Nucleic Acids Res.*, **48**, 3156–3164.
42. Lin, W., Ma, J., Nong, D., Xu, C., Zhang, B., Li, J., Jia, Q., Dou, S., Ye, F., Xi, X. *et al.* (2017) Helicase stepping investigated with one-nucleotide resolution fluorescence resonance energy transfer. *Phys. Rev. Lett.*, **119**, 138102.
43. MacKerell, Jr., Brooks, A.D., Brooks, B., Nilsson, C.L., Roux, L., Won, B. and Karplus, M. (1998b) In: *The Encyclopedia of Computational Chemistry*. John Wiley & Sons, Chichester, UK.
44. Zoete, V., Cuendet, M.A., Grosdidier, A. and Michielin, O. (2011) SwissParam: a fast force field generation tool for small organic molecules. *J. Comput. Chem.*, **32**, 2359–2368.
45. Bussi, G., Donadio, D. and Parrinello, M. (2007) Canonical sampling through velocity-rescaling. *J. Chem. Phys.*, **126**, 014101.
46. Parrinello, M. and Rahman, A. (1981) Polymorphic transitions in single crystals: a new molecular dynamics method. *J. Appl. Phys.*, **52**, 7182–7190.
47. Baker, N.A., Sept, D., Joseph, S., Holst, M.J. and McCammon, J.A. (2001) Electrostatics of nanosystems: application to microtubules and the ribosome. *Proc. Natl. Acad. Sci. U.S.A.*, **98**, 10037–10041.
48. Pettersen, E.F., Goddard, T.D., Huang, C.C., Couch, G.S., Greenblatt, D.M., Meng, E.C. and Ferrin, T.E. (2004) UCSF Chimera—a visualization system for exploratory research and analysis. *J. Comput. Chem.*, **25**, 1605–1612.
49. Lerner, E., Barth, A., Hendrix, J., Ambrose, B., Birkedal, V., Blanchard, S.C., Börner, R., Chung, S.H., Cordes, T., Craggs, T.D. *et al.* (2021) FRET-based dynamic structural biology: Challenges, perspectives and an appeal for open-science practices. *Elife*, **10**, e60416.
50. Kalinin, S., Peulen, T., Sindbert, S., Rothwell, P.J., Berger, S., Restle, T., Goody, R.S., Gohlke, H. and Seidel, C.A.M. (2012) A toolkit and benchmark study for FRET-restrained high-precision structural modeling. *Nat. Methods*, **9**, 1218–1225.
51. Li, J.H., Lin, W.X., Zhang, B., Nong, D.G., Ju, H.P., Ma, J.B., Xu, C.H., Ye, F.F., Xi, X.G., Li, M. *et al.* (2016) Pif1 is a force-regulated helicase. *Nucleic Acids Res.*, **44**, 4330–4339.
52. Harami, G.M., Seol, Y., In, J., Ferencziová, V., Martina, M., Gyimesi, M., Sarlós, K., Kovács, Z.J., Nagy, N.T., Sun, Y. *et al.* (2017) Shuttling along DNA and directed processing of D-loops by RecQ helicase support quality control of homologous recombination. *Proc. Natl. Acad. Sci. U.S.A.*, **114**, E466–E475.
53. Ribbeck, N., Kaplan, D.L., Bruck, I. and Saleh, O.A. (2010) DnaB helicase activity is modulated by DNA geometry and force. *Biophys. J.*, **99**, 2170–2179.
54. Johnson, D.S., Bai, L., Smith, B.Y., Patel, S.S. and Wang, M.D. (2007) Single-molecule studies reveal dynamics of DNA unwinding by the ring-shaped T7 helicase. *Cell*, **129**, 1299–1309.
55. Lionnet, T., Spiering, M.M., Benkovic, S.J., Bensimon, D. and Croquette, V. (2007) Real-time observation of bacteriophage T4 gp41 helicase reveals an unwinding mechanism. *Proc. Natl. Acad. Sci. U.S.A.*, **104**, 19790–19795.
56. Lee, K.S., Balci, H., Jia, H., Lohman, T.M. and Ha, T. (2013) Direct imaging of single UvrD helicase dynamics on long single-stranded DNA. *Nat. Comm.*, **4**, 1878.
57. Byrd, A.K., Matlock, D.L., Bagchi, D., Aarattuthodiyil, S., Harrison, D., Croquette, V. and Raney, K.D. (2012) Dda helicase tightly couples translocation on single-stranded DNA to unwinding of duplex DNA: Dda is an optimally active helicase. *J. Mol. Biol.*, **420**, 141–154.
58. Sun, B., Wei, K.J., Zhang, B., Zhang, X.H., Dou, S.X., Li, M. and Xi, X.G. (2008) Impediment of *E. coli* UvrD by DNA-destabilizing

- force reveals a strained-inchworm mechanism of DNA unwinding. *EMBO J.*, **27**, 3279–3287.
59. Zhou, R., Zhang, J., Bochman, M.L., Zakian, V.A. and Ha, T. (2014) Periodic DNA patrolling underlies diverse functions of Pif1 on R-loops and G-rich DNA. *Elife*, **3**, e02190.
60. Ramanagoudr-Bhojappa, R., Chib, S., Byrd, A.K., Aarattuthodiyil, S., Pandey, M., Patel, S.S. and Raney, K.D. (2013) Yeast Pif1 helicase exhibits a one-base-pair stepping mechanism for unwinding duplex DNA. *J. Biol. Chem.*, **288**, 16185–16195.
61. Rieu, M., Valle-Oretero, J., Ducos, B., Allemand, J.-F. and Croquette, V. (2021) Single-molecule kinetic locking allows fluorescence-free quantification of protein/nucleic-acid binding. *Commun. Biol.*, **4**, 1083.
62. Bell, G.I. (1978) Models for the specific adhesion of cells to cells. *Science*, **200**, 618–627.
63. Vacic, V., Uversky, V.N., Dunker, A.K. and Lonardi, S. (2007) Composition Profiler: a tool for discovery and visualization of amino acid composition differences. *BMC Bioinf.*, **8**, 211.
64. Levin, M.K. and Patel, S.S. (2002) Helicase from hepatitis C virus, energetics of DNA binding. *J. Biol. Chem.*, **277**, 29377–29385.
65. Leila, S., Boriani, M., Charles, C.R. and Mark, C.W. (2006) (*ed. March, A. P. S.*) *Meeting*. Baltimore, MD.
66. Lahaye, A., Leterme, S. and Foury, F. (1993) PIF1 DNA helicase from *Saccharomyces cerevisiae*. *J. Biol. Chem.*, **268**, 26155–26161.
67. Sun, B., Johnson, D.S., Patel, G., Smith, B.Y., Pandey, M., Patel, S.S. and Wang, M.D. (2011) ATP-induced helicase slippage reveals highly coordinated subunits. *Nature*, **478**, 132–135.